An Efficient 3-D Spectral-Element Method for Schrödinger Equation in Nanodevice Simulation

Joon-Ho Lee and Qing Huo Liu, *Fellow, IEEE*

***Abstract*—A three-dimensional (3-D) spectral-element method (SEM) based on Gauss–Lobatto–Legendre (GLL) polynomials is proposed to solve the Schrödinger equation in nanodevice simulation. Galerkin's method is employed to obtain the system equation. The high-order basis functions employed are orthogonal and the numerical quadrature points are the same as the GLL integration points, leading to a diagonal mass matrix and a more sparse stiffness matrix. Thus, the proposed method leads to a regular eigenvalue problem, rather than a generalized eigenvalue problem, greatly reducing the computer-memory requirement and central-processing-unit (CPU) time in comparison with the conventional finite-element method (FEM). Furthermore, the SEM is implemented for high geometrical orders, where curved structures can be modeled up to the accuracy comparable to the interpolation accuracy afforded by the basis functions. Numerical examples verify a spectral accuracy with the interpolation orders, and confirm that higher geometrical orders are essential for curved structures to achieve overall spectral accuracy. Examples of quantum dots in various structures, including a waveguide, are analyzed with mixed boundary conditions. Numerical results show that the SEM is an efficient alternative to conventional FEM and to the finite-difference method (FDM) for nanodevice simulation.**

***Index Terms*—Galerkin's method, Gauss–Lobatto–Legendre (GLL) interpolation, nanodevices, quantum dot, Schrödinger equation, spectral-element method (SEM).**

I. Introduction

As quantum effects are critical in the understanding and design optimization of nanodevices, the numerical solution of Schrödinger's equation becomes increasingly important. Many researchers have successfully developed various numerical methods for this purpose, for example, [1]. In particular, three-dimensional (3-D) solutions of Schrödinger equation or self-consistent Schrödinger–Poisson system have attracted much attention recently (see, for example, [2]–[7]). It has been noted that some quantum effects can only be explained if a 3-D model is used [3].

Previously, for one-dimensional (1-D) problems, several methods have been employed to solve Schrödinger's equation, including analytical methods such as phase-shift analysis [8] and Airy function methods with real and complex arguments [9]–[12], and numerical methods such as variational methods [13], finite-element method [14], finite-difference method [15]–[18], Green function [19], stabilization graph [20], [21], Fourier series [21], complex coordinates [22], and optical-potential wave-packet propagation method [23]. As an efficient alternative, we have introduced a spectral-grid method (SGM) [24] that utilizes the Chebyshev pseudospectral method as it was employed in computational electromagnetics [25]. We have shown that the numerical accuracy of the SGM is far superior to the conventional finite-element and finite-difference methods in 1-D examples. More recently, we have extended this idea to the Galerkin formulation in the spectral-element framework, and applied the method to solve the 1-D self-consistent Schrödinger–Poisson system [26]. Compared to the SGM [25], this spectral-element method (SEM) [26] is easier to implement at the boundaries between elements.

In this paper, we further extend the SEM to solve the 3-D Schrödinger equation. One important difference between 1-D and 3-D problems is that the problem geometry in 3-D can be curved. Under this situation, we show that it is essential that the curved geometry is accurately represented up to high orders, in order to achieve the spectral accuracy of the method. This paper can be considered as extensions of similar ideas in electromagnetics and elastodynamics in the time domain [27]–[32]. It is a direct extension of our work on the electromagnetic eigenvalue solver reported in [33]. Although we focus on the Schrödinger equation in this paper, it is natural for us to extend this to the self-consistent Schrödinger–Poisson system in 3-D in our future work, as has been done in the 1-D case [26].

The organization of this paper is as follows. In Section II, we will present the detailed formulation of the SEM. This will be followed by the high-order model in curved 3-D structures in Section III. Finally, we will present numerical examples in Section IV to demonstrate the capability of the SEM.

II. Formulation

For the convenience of numerical computation, we consider the normalized Schrödinger equation

$$-\frac{1}{\pi^2}\nabla\cdot\left(\frac{1}{m}\nabla\varphi\right)+(V-E)\varphi=f \tag{1}$$

where φ is the wave function, m the effective mass normalized by the mass density m_0 of the electron, V the potential normalized by E_0 (here we choose $E_0=\hbar^2\pi^2/2m_0d^2$ as the eigenenergy of the electron in an infinite quantum well of width d), E the eigenenergy normalized by E_0, and f is the incoming electron source [24].

Manuscript received December 20, 2004; revised February 17, 2005. This work was supported by a grant from the Semiconductor Research Corporation. This paper was recommended by Associate Editor H. Kosina.

The authors are with the Department of Electrical and Computer Engineering, Duke University, Durham NC 27708-0291 USA (e-mail: jhlee@ee.duke.edu; qhliu@ee.duke.edu).

Digital Object Identifier 10.1109/TCAD.2005.852675

The boundary conditions to be considered can be described by

$$\frac{1}{\pi^2 m}\frac{\partial \varphi}{\partial n} + \gamma\varphi = q \tag{2}$$

where γ and q are known parameters associated with the physical properties of the boundary. It is noted that both Dirichlet ($\gamma \to \infty$, $q = 0$), Neumann ($\gamma = 0$, $q = 0$), and the one-way wave conditions are special cases of this equation. The goal of this work is to develop an SEM for the efficient solution of this Schrödinger equation.

A. Basis Functions on a Reference Element

The SEM is characterized by its spectral accuracy, i.e., the error decreases exponentially with the order of basis functions. In order to achieve spectral accuracy, we introduce a Gauss–Lobatto–Legendre (GLL) element discretization for Schrödinger equation (1). The Nth order GLL basis functions in a 1-D standard reference element $\xi \in [-1, 1]$ are defined by

$$\phi_j^{(N)}(\xi) = \frac{-1}{N(N+1)L_N(\xi_j)}\frac{(1-\xi^2)L'_N(\xi)}{(\xi - \xi_j)} \tag{3}$$

for $j = 0, \ldots, N$, where $L_N(\xi)$ is the Legendre polynomial of Nth order and $L'_N(\xi)$ is its derivative. The grid points $\{\xi_j, j = 0, 1, \ldots, N\}$ within the element $\xi \in [-1, 1]$ are chosen as the GLL points, i.e., the zeros of $(1-\xi^2)L'_N(\xi_j) = 0$. Using (3) as an interpolation function, an arbitrary smooth function $f(\xi)$ can be written as

$$f(\xi) = \sum_{j=0}^{N} f(\xi_j)\phi_j^{(N)}(\xi) \tag{4}$$

with an error of $O(\Delta\xi^{N+1})$, where $\Delta\xi$ is the average increment of the grid points. By definition, the above Lagrange–Legendre interpolation has the fundamental property

$$\phi_j(\xi_i) = \delta_{ji} \tag{5}$$

which greatly simplifies the implementation of the SEM.

Moreover, the integration of a function can be written as

$$\int_{-1}^{1} f(\xi)\mathrm{d}\xi = \sum_{j=0}^{N} w_j^{(N)} f(\xi_j) \tag{6}$$

with an error of $O(\Delta\xi^{2N-1})$, where the weights for the numerical quadrature integration are

$$w_j^{(N)} = \frac{2}{N(N+1)L_N^2(\xi_j)}. \tag{7}$$

On a 3-D standard reference element, i.e., a cubic element $(\xi, \eta, \zeta) \in [-1, 1] \times [-1, 1] \times [-1, 1]$, the basis functions can be written as

$$\phi_{rst} = \phi_r^{(N_\xi)}(\xi)\phi_s^{(N_\eta)}(\eta)\phi_t^{(N_\zeta)}(\zeta) \tag{8}$$

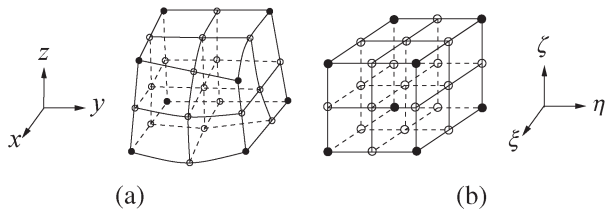

Fig. 1. A general curved hexahedron in the (a) physical and (b) reference domains. In general, high-order polynomials will be used for this mapping, but for clarity here only the second-order mapping ($M_\xi = M_\eta = M_\zeta = 2$) is shown.

for $r = 0, \ldots, N_\xi$; $s = 0, \ldots, N_\eta$; $t = 0, \ldots, N_\zeta$. The interpolation and integration of a function $f(\xi, \eta, \zeta)$ can be written as

$$f(\xi, \eta, \zeta) = \sum_{r=0}^{N_\xi}\sum_{s=0}^{N_\eta}\sum_{t=0}^{N_\zeta} f(\xi_r, \eta_s, \zeta_t) \times \phi_r^{(N_\xi)}(\xi)\phi_s^{(N_\eta)}(\eta)\phi_t^{(N_\zeta)}(\zeta) \tag{9}$$

$$\int_{-1}^{1}\int_{-1}^{1}\int_{-1}^{1} f(\xi, \eta, \zeta)\mathrm{d}\xi\mathrm{d}\eta\mathrm{d}\zeta = \sum_{r=0}^{N_\xi}\sum_{s=0}^{N_\eta}\sum_{t=0}^{N_\zeta} w_r^{(N_\xi)} w_s^{(N_\eta)} w_t^{(N_\zeta)} f(\xi_r, \eta_s, \zeta_t). \tag{10}$$

B. Division of Physical Domain Into Elements

The basis functions presented above are for a standard cubic reference element in 3-D. For complex problems, the physical domain is first subdivided into a set of nonoverlapping generally curved hexahedron elements. Each such hexahedron element in Cartesian coordinates (x, y, z) is mapped into a reference cubic element in (ξ, η, ζ) coordinates through an invertible curvilinear coordinate transformation. As an example, a curved hexahedron element is mapped into a reference (standard) element in Fig. 1. In general, the curved hexahedron can be accurately transformed into a cube through high-order curvilinear mapping, as will be discussed in more detail in Section III. In the example in Fig. 1, for clarity we only show a curved cube modeled by a quadratic mapping.

In the reference element, we consider the wave function $\varphi(\xi, \eta, \zeta)$. This reference element is discretized by $(N_\xi + 1)(N_\eta + 1)(N_\zeta + 1)$ GLL points $\{\xi_r; \eta_s; \zeta_t; r = 0, \ldots, N_\xi; s = 0, \ldots, N_\eta; t = 0, \ldots, N_\zeta\}$, where ξ_r, η_s, and ζ_t represent the locations of GLL grid points in the ξ, η, and ζ directions, respectively. Consequently, the wave function can be represented by the tensor product of Lagrange–Legendre interpolation polynomials as

$$\varphi(\xi, \eta, \zeta) = \sum_{r=0}^{N_\xi}\sum_{s=0}^{N_\eta}\sum_{t=0}^{N_\zeta} \varphi(\xi_r, \eta_s, \zeta_t)\phi_r(\xi)\phi_s(\eta)\phi_t(\zeta) \equiv \sum_{j=1}^{N} \varphi_j \Psi_j \tag{11}$$

where N_ξ, N_η, and N_ζ are interpolation orders of the reference domain along ξ, η, and ζ parametric coordinates, respectively, $N = (N_\xi + 1)(N_\eta + 1)(N_\zeta + 1)$ is the total number of points in the reference element, and $\Psi_j = \varphi_r(\xi)\varphi_s(\eta)\varphi_t(\zeta)$ is the basis function.

C. Galerkin Weighted-Residual Formulation

The residual of (1) is

$$r = -\frac{1}{\pi^2}\nabla\cdot\left(\frac{1}{m}\nabla\varphi\right) + (V - E)\varphi - f. \tag{12}$$

The Galerkin weighted-residual method is applied to minimize the residual (12) over the entire region. It can be expressed in the eth element as

$$R_i^e = \int_{v_e} \Psi_i r \mathrm{d}v, \qquad i = 1, 2, \ldots, N. \tag{13}$$

Substituting the wave function (11) into (13) yields

$$\begin{aligned} R_i^e = \sum_{j=1}^{N} \int_{v_e} \Bigg[& \frac{1}{\pi^2}(\nabla\Psi_i)\cdot\left(\frac{1}{m}\nabla\Psi_j\right)\varphi_j \\ & + (V - E)\Psi_i\Psi_j\varphi_j - \Psi_i f \Bigg] \mathrm{d}v \\ - \sum_{j=1}^{N_b} \oint_{\Gamma_e} & \frac{1}{\pi^2 m}\frac{\partial\Psi_i}{\partial n}\varphi_j \mathrm{d}s \end{aligned} \tag{14}$$

where N_b is the number of boundary nodes in the eth element. If homogeneous boundary conditions are applied, the boundary integral terms will vanish.

Applying (14) to all elements, and using (2), we have a discretized system of equations in the reference domain

$$\begin{aligned} & \sum_{e=1}^{K}\sum_{j=1}^{N}\int_{-1}^{1}\int_{-1}^{1}\int_{-1}^{1} \frac{1}{\pi^2}(\nabla\Psi_i)\cdot\mathbf{J}_e^{-T}\mathbf{J}_e^{-1}\left(\frac{1}{m}\nabla\Psi_j\right)\varphi_j|\mathbf{J}_e|\mathrm{d}\xi\mathrm{d}\eta\mathrm{d}\zeta \\ & + \sum_{e=1}^{K}\sum_{j=1}^{N}\int_{-1}^{1}\int_{-1}^{1}\int_{-1}^{1}(V - E)\Psi_i\Psi_j\varphi_j|\mathbf{J}_e|\mathrm{d}\xi\mathrm{d}\eta\mathrm{d}\zeta \\ & + \sum_{b=1}^{K_b}\sum_{j=1}^{N_b}\int_{-1}^{1}\int_{-1}^{1}\gamma\Psi_i\Psi_j\varphi_j|\mathbf{J}_b|\mathrm{d}u\mathrm{d}v \\ & = \sum_{e=1}^{K}\int_{-1}^{1}\int_{-1}^{1}\int_{-1}^{1} f\Psi_i|\mathbf{J}_e|\mathrm{d}\xi\mathrm{d}\eta\mathrm{d} + \sum_{b=1}^{K_b}\int_{-1}^{1}\int_{-1}^{1} q\Psi_i|\mathbf{J}_b|\mathrm{d}u\mathrm{d}v \end{aligned} \tag{15}$$

where $i = 1, 2, \ldots, N$; K is the number of elements, K_b is the number of boundary elements, $\mathbf{J}_e$ is the Jacobian matrix associated with the mapping from an element to the reference domain, $\mathbf{J}_b$ is the Jacobian matrix for the surface reference domain (it is a special case of $\mathbf{J}_e$ on the boundary), and (u, v) are the reference coordinates on the boundary. The gradient in (15) is computed in the reference domain

$$\begin{aligned} \nabla\Psi &= \nabla\left(\phi_r(\xi)\phi_s(\eta)\phi_t(\zeta)\right) \\ &= \hat{\xi}\phi_r'(\xi)\phi_s(\eta)\phi_t(\zeta) + \hat{\eta}\phi_r(\xi)\phi_s'(\eta)\phi_t(\zeta) \\ &\quad + \hat{\zeta}\phi_r(\xi)\phi_s(\eta)\phi_t'(\zeta) \end{aligned} \tag{16}$$

where ϕ' denotes the derivative of the Lagrange–Legendre interpolation polynomials with respect to the reference coordinate. After this spatial discretization with spectral elements, we can rewrite (15) in matrix form as

$$(\mathbf{A} + \mathbf{B} + \mathbf{G})\varphi = \mathbf{F} + \mathbf{Q} \tag{17}$$

where $\mathbf{A}$ is the stiffness matrix, $\mathbf{B} = \mathbf{B}_1 - E\mathbf{B}_2$ is the mass matrix, $\mathbf{B}_1$ is related to the normalized potential V, $E\mathbf{B}_2$ is related to the normalized energy E, $\mathbf{G}$ is the boundary integral matrix, $\mathbf{F}$ is the forcing vector, and $\mathbf{Q}$ is the boundary source vector arising from the boundary condition in (2). As shown next, since the element basis functions are orthogonal, we can obtain the diagonal mass matrix, which is an important property of the SEM.

D. Numerical Integration

To obtain the system (17), numerical integration should be used in (15). If the element is straight, (15) involves a polynomial of degree $2N$ because of the product of two polynomials of degree N; if the element is curved, the integrand is a function of order higher than $2N$. The GLL quadrature is exact for the integration of polynomials of order $2N - 1$ [34]. Therefore, exact evaluation of the stiffness matrix and mass matrix requires increasing the number of GLL points up to $N + 1$ (or more for curved elements), which results in a nondiagonal mass matrix.

For examples, in a straight element, the stiffness matrix includes an integration

$$A'_{ij} = \int_{-1}^{1}\int_{-1}^{1}\int_{-1}^{1} \phi_m'^{(N_\xi)}\phi_n^{(N_\eta)}\phi_p^{(N_\zeta)}\phi_{m'}'^{(N_\xi)}\phi_{n'}^{(N_\eta)}\phi_{p'}^{(N_\zeta)}\mathrm{d}\xi\mathrm{d}\eta\mathrm{d}\zeta \tag{18}$$

and the mass matrix includes an integration

$$B'_{ij} = \int_{-1}^{1}\int_{-1}^{1}\int_{-1}^{1} \phi_m^{(N_\xi)}\phi_n^{(N_\eta)}\phi_p^{(N_\zeta)}\phi_{m'}^{(N_\xi)}\phi_{n'}^{(N_\eta)}\phi_{p'}^{(N_\zeta)}\mathrm{d}\xi\mathrm{d}\eta\mathrm{d}\zeta \tag{19}$$

where i is a compound index of (m, n, p) and j is a compound index of (m', n', p'). The exact evaluation of these two integrations can be expressed in terms of the (N_ξ, $N_{\eta+1}$,

TABLE I
ANALYTICAL EIGENVALUE SOLUTIONS OF THE LOWEST SEVEN MODES FOR A CUBE MODEL

Mode 1	Modes 2, 3, 4	Modes 5, 6, 7
0.75	1.5	2.25

$N_\zeta + 1$)th-order and ($N_\xi + 1$, $N_\eta + 1$, $N_\zeta + 1$)th-order GLL quadrature, respectively

$$A'_{ij} = \sum_{r=0}^{N_\xi} \sum_{s=0}^{N_\eta+1} \sum_{t=0}^{N_\zeta+1} w_r^{(N_\xi)} w_s^{(N_\eta+1)} w_t^{(N_\zeta+1)} \times \phi_m'^{(N_\xi)}(\xi_r)\phi_{m'}'^{(N_\xi)}(\xi_r)\phi_n^{(N_\eta)}(\eta_s)\phi_{n'}^{(N_\eta)}(\eta_s) \times \phi_p^{(N_\zeta)}(\zeta_t)\phi_{p'}^{(N_\zeta)}(\zeta_t) \quad (20)$$

$$B'_{ij} = \sum_{r=0}^{N_\xi+1} \sum_{s=0}^{N_\eta+1} \sum_{t=0}^{N_\zeta+1} w_r^{(N_\xi+1)} w_s^{(N_\eta+1)} w_t^{(N_\zeta+1)} \times \phi_m^{(N_\xi)}(\xi_r)\phi_{m'}^{(N_\xi)}(\xi_r)\phi_n^{(N_\eta)}(\eta_s)\phi_{n'}^{(N_\eta)}(\eta_s) \times \phi_p^{(N_\zeta)}(\zeta_t)\phi_{p'}^{(N_\zeta)}(\zeta_t). \quad (21)$$

On the other hand, if we only use (N_ξ, N_η, N_ζ) orders for the GLL quadrature, the approximate evaluation of the two integrations can be simplified as

$$A'_{ij} \simeq \sum_{r=0}^{N_\xi} \sum_{s=0}^{N_\eta} \sum_{t=0}^{N_\zeta} w_r^{(N_\xi)} w_s^{(N_\eta)} w_t^{(N_\zeta)} \times \phi_m'^{(N_\xi)}\phi_{m'}'^{(N_\xi)}\phi_n^{(N_\eta)}\phi_{n'}^{(N_\eta)}\phi_p^{(N_\zeta)}\phi_{p'}^{(N_\zeta)} = \delta_{nn'}\delta_{pp'} w_n^{(N_\eta)} w_p^{(N_\zeta)} \sum_{r=0}^{N_\xi} w_m^{(N_\xi)} \phi_m'^{(N_\xi)} \phi_{m'}'^{(N_\xi)} \quad (22)$$

$$B'_{ij} \simeq \sum_{r=0}^{N_\xi} \sum_{s=0}^{N_\eta} \sum_{t=0}^{N_\zeta} w_r^{(N_\xi)} w_s^{(N_\eta)} w_t^{(N_\zeta)} \times \phi_m^{(N_\xi)}\phi_{m'}^{(N_\xi)}\phi_n^{(N_\eta)}\phi_{n'}^{(N_\eta)}\phi_p^{(N_\zeta)}\phi_{p'}^{(N_\zeta)} = \delta_{mm'}\delta_{nn'}\delta_{pp'} w_m^{(N_\xi)} w_n^{(N_\eta)} w_p^{(N_\zeta)}. \quad (23)$$

The stiffness and mass matrix by the approximate integrations require $O(N^{7/3})$ and $O(N)$ operations, respectively, while those by the exact integrations require $O(N^3)$ and $O(N^3)$ operations, respectively. In addition, the approximate integrations give a diagonal mass matrix. Therefore, the approximate integrations require less central-processing-unit (CPU) time and computer memory than the exact integrations, but the exact integrations give a more accurate evaluation of the matrices (for curved elements, it is also only approximate). In the numerical examples in the next section, we will investigate which integration method is more efficient, given a fixed accuracy. For error estimates and convergence properties of the spectral and pseudospectral methods, the reader is referred to [36]–[39].

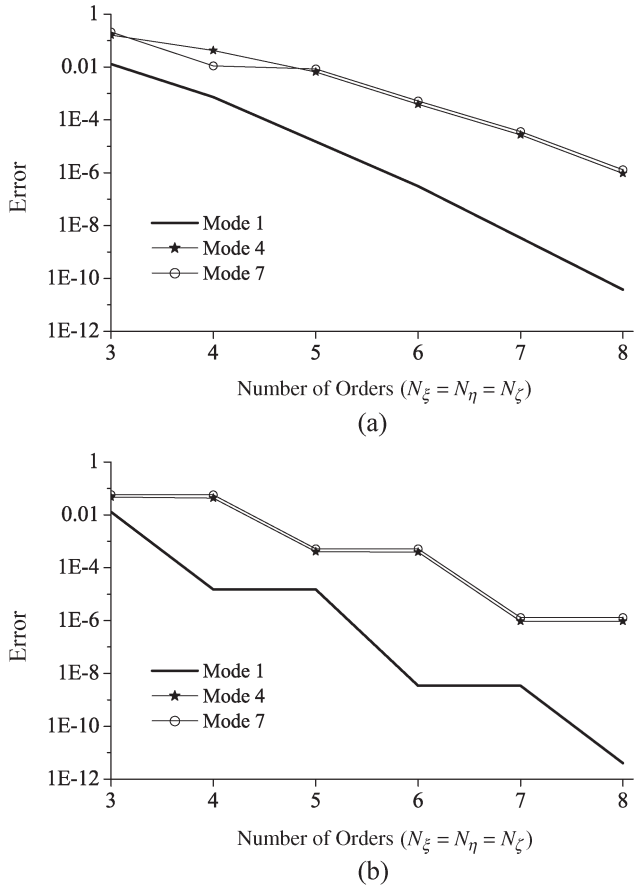

Fig. 2. Error of eigenvalues obtained by (a) approximate and (b) exact integration of stiffness and mass matrices for one element. The normalized effective mass m is 1, and the normalized potential V is 0. The Dirichlet boundary condition was applied to all outer boundaries.

III. HIGHER ORDER GEOMETRICAL MODELING

In the traditional weighted-residual method, the problem geometry is modeled by the first-order approximation (i.e., straight elements), leading to at best a second-order accurate solution no matter how high the interpolation order used for curved geometries. As a result, unfortunately, in most applications, the accuracy is usually limited by a geometry representation, rather than the basis functions. To achieve higher order accuracy, more accurate geometrical representation is required. Here, we employ a higher order geometrical modeling technique to provide accuracy and efficiency of the analysis in practical applications.

During geometrical modeling, we use generalized curved parametric hexahedrons of higher geometrical order [35]. A general curved-hexahedron element can be described approximately as

$$\mathbf{r}(\xi,\eta,\zeta) = \sum_{i=1}^{M} \mathbf{r}_i L_i^{(M)}(\xi,\eta,\zeta) = \sum_{r=0}^{M_\xi} \sum_{s=0}^{M_\eta} \sum_{t=0}^{M_\zeta} \mathbf{r}_{rst} L_r^{(M_\xi)}(\xi) L_s^{(M_\eta)}(\eta) L_t^{(M_\zeta)}(\zeta), \quad -1 \le \xi,\eta,\zeta \le 1 \quad (24)$$

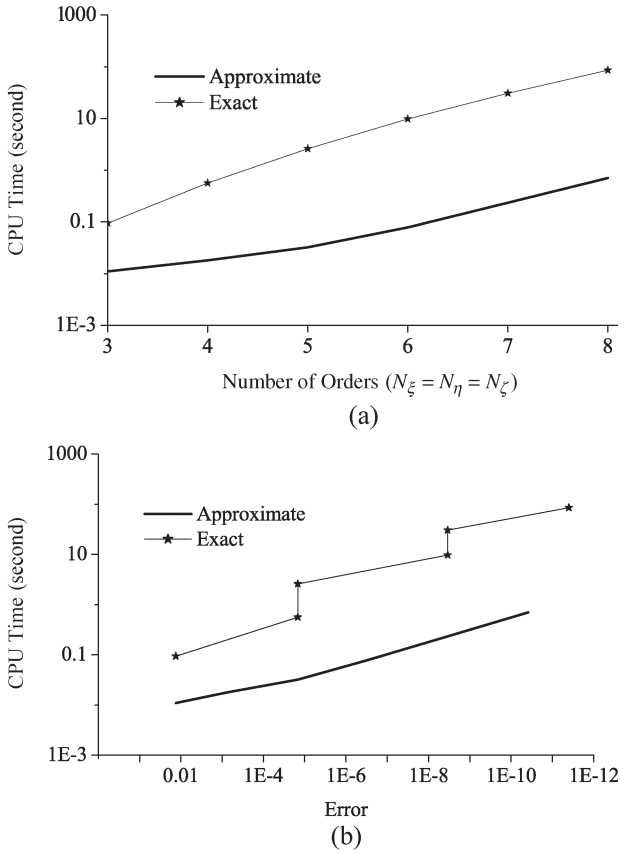

Fig. 3. Comparison of (a) CPU time and (b) efficiency for exact and approximate integrations.

TABLE II
COMPARISON OF EFFICIENCY AND ACCURACY BETWEEN THE SEM AND THE CONVENTIONAL FEM

Method	Orders $N_\xi = N_\eta = N_\zeta$	Error (percentage)	CPU Time (second)	Memory (kilobyte)
FEM	1	0.825	3.291	4564
SEM	4	0.073	0.016	7

where M_ξ, M_η, and M_ζ are geometrical orders of an element along ξ-, η-, and ζ- parametric coordinates, respectively, $M = (M_\xi + 1)(M_\eta + 1)(M_\zeta + 1)$ is the total number of points, $\mathbf{r}_i$ is the position vector of the interpolation points, $i = m + n(M_\xi + 1) + p(M_\xi + 1)(M_\eta + 1) + 1$, and $L_r^{M_\xi}$, $L_s^{M_\eta}$, and $L_t^{M_\zeta}$ represent Lagrange interpolating polynomials. Increasing orders (M_ξ, M_η, M_ζ) will lead to an improved accuracy in geometrical modeling.

We have used the scheme in (24) and model curved elements up to the order of $(M_\xi, M_\eta, M_\zeta) = (9, 9, 9)$. For clarity, Fig. 1 shows the second-order geometrical modeling where the structure is determined by 27 points. In order to make a realistic modeling, we allow different geometrical orders in the same mesh so that high orders are used only for the curved subdomain.

As will be shown in the next section, the combined high-order modeling of the geometry and basis functions provide a spectral accuracy in the SEM.

TABLE III
ANALYTIC EIGENVALUE SOLUTIONS OF THE LOWEST TEN MODES FOR A SPHERE OF RADIUS $a = 1$ nm

Mode	ka	n	Mode	ka	n
1	3.14159	0	6	7.72525	1
2	4.49341	1	7	8.18256	4
3	5.76346	2	8	9.09501	2
4	6.28319	0	9	9.35581	5
5	6.98793	3	10	9.42478	0

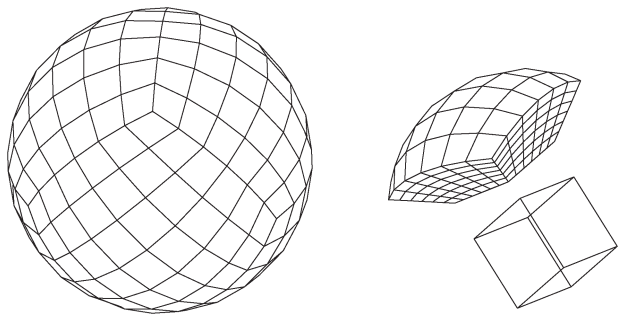

Fig. 4. The curved mesh of the sphere model. This mesh consists of six curved outer elements and one straight cubic element at the center.

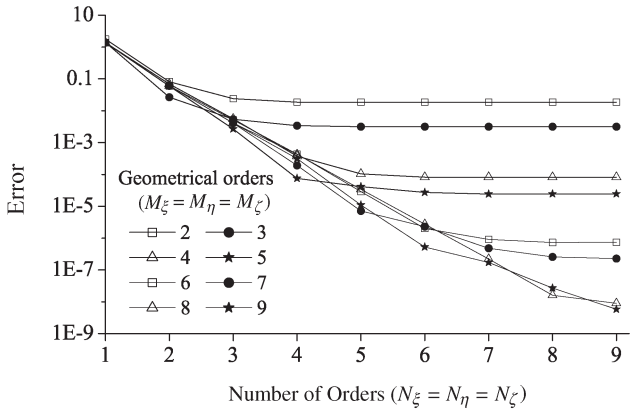

Fig. 5. Errors of the fundamental eigenvalue for various geometrical orders. GLL points are employed as the geometrical interpolation points.

IV. NUMERICAL EXAMPLES AND DISCUSSIONS

A. Test Models

In order to verify its accuracy and efficiency, we applied the proposed SEM to numerous test models; below we show two such models. These models are generalized eigenvalue problems for the Schrödinger equation with Dirichlet boundary condition; they can be obtained by letting $\mathbf{G} = 0$, $\mathbf{F} = 0$, and $\mathbf{Q} = 0$ in (17)

$$(\mathbf{A} + \mathbf{B}_1)\varphi = E\mathbf{B}_2\varphi. \tag{25}$$

As we noted earlier, if an exact method is used, $\mathbf{B}_1$ and $\mathbf{B}_2$ are full matrices within each element. On the other hand, if we use the (N_ξ, N_η, N_ζ)th-order GLL quadrature, i.e., the approximate integration, these matrices are diagonal. In the latter case, it can be converted to a regular eigenvalue problem

$$\widetilde{\mathbf{A}}\widetilde{\varphi} = E\widetilde{\varphi} \tag{26}$$

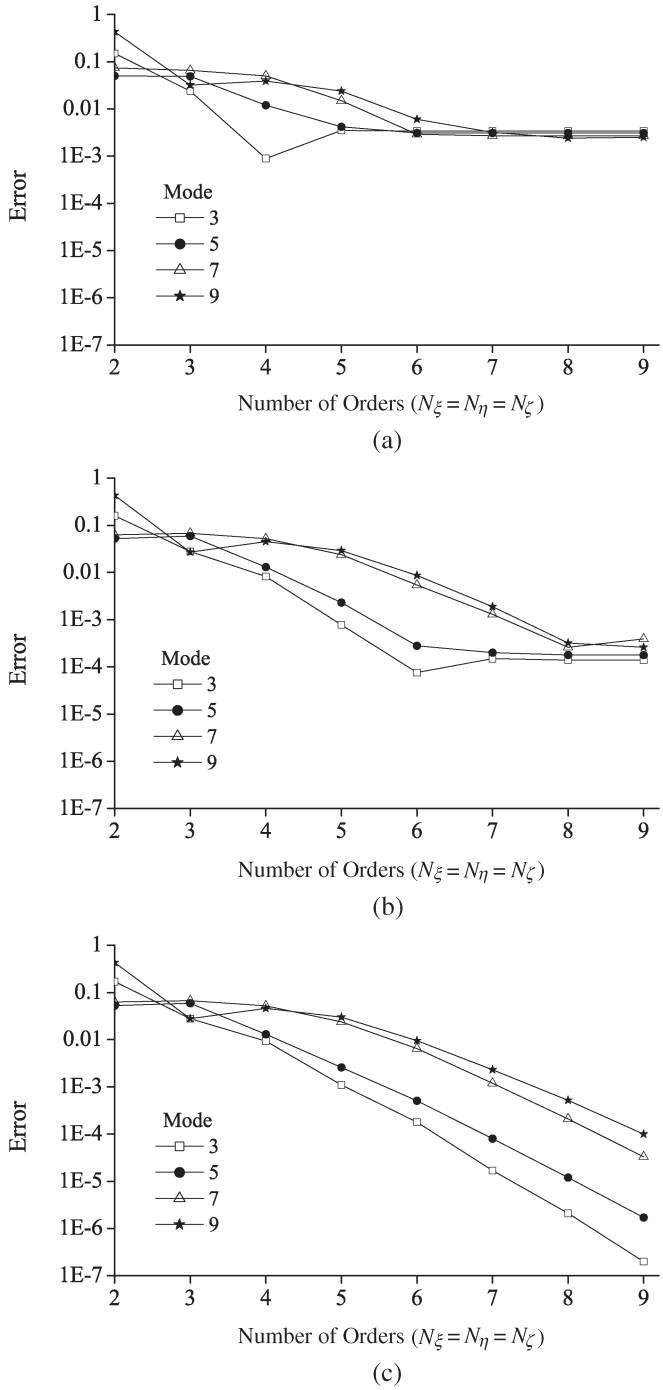

Fig. 6. Errors of higher eigenvalues versus the order of basis functions. Geometrical orders ($M_\xi = M_\eta = M_\zeta$) are (a) 3, (b) 5, and (c) 9.

where $\widetilde{\varphi} = \mathbf{B}_2^{1/2}\varphi$ and

$$\widetilde{\mathbf{A}} = \mathbf{B}_2^{-\frac{1}{2}}(\mathbf{A} + \mathbf{B}_1)\mathbf{B}_2^{-\frac{1}{2}}. \tag{27}$$

Such a regular eigenvalue problem is much more desirable than the generalized eigenvalue problem because of its reduced computational cost.

The first example is a homogeneous-cube model with dimensions $2\ \mathrm{nm} \times 2\ \mathrm{nm} \times 2\ \mathrm{nm}$, with $V = 0$ inside the cube. It is modeled by a single trilinear hexahedron element. Table I shows the first three eigenvalues obtained by analytical solutions. The relative errors of the eigenvalues obtained by the SEM are shown in Fig. 2(a) and (b) versus the orders $N_\xi = N_\eta = N_\zeta$ when the integrations are obtained by exact and approximate methods, respectively. Both figures confirm that the proposed SEM has exponential accuracy with increasing order in the basis functions. In the approximate-integration method, the error is, overall, a straight line in the semilog plot; for the exact integration, the errors are also straight lines if one groups the even and odd orders separately, and the even and odd orders have different constant offsets. The exact integration gives slightly more accurate results than approximate integration. It is also observed that although the exact integration is slightly more accurate, its accuracy is in the same order as the approximate integration.

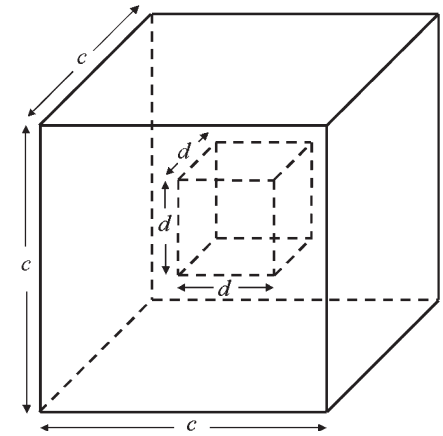

Fig. 7. A cubic quantum dot with $V = 0$ and $m = 2$ surrounded by a cubic outer shell with $V = 2$ and $m = 1$. The size of $c = 3$ nm and $d = 1$ nm.

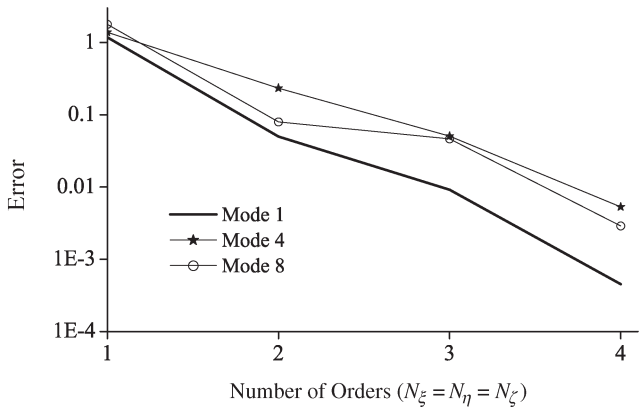

Fig. 8. Errors of eigenvalues obtained by the second-, third-, and fourth-order basis functions with 27 orthogonal elements for the cube.

On the other hand, we compared the CPU time consumed by the approximate integration and the exact integration in Fig. 3(a). We observe that approximate integration is superior to exact integration. The CPU time of approximate integration is less than 1% of that consumed by exact integration when the order of basis functions is 8.

Next, in Fig. 3(b), we compared the CPU time between the two integrations versus the accuracy. From the figure, we observe that approximate integration is much more efficient

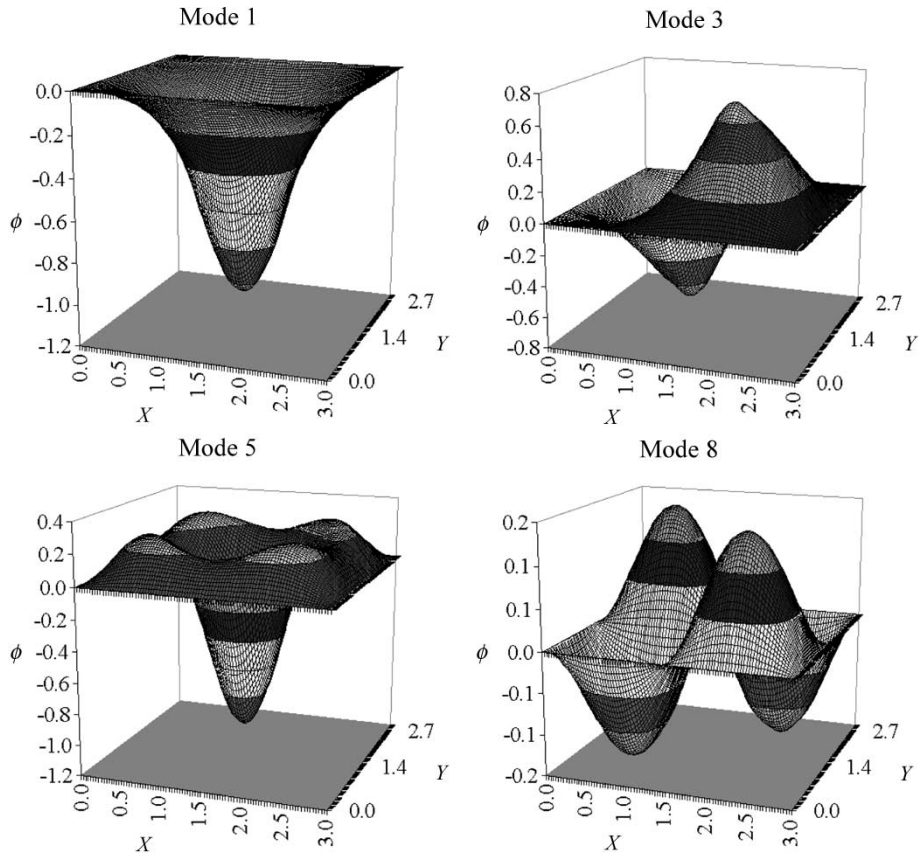

Fig. 9. Eigenvectors of modes 1, 3, 5, and 8 with the fifth-order basis functions. The normalized effective mass is 1 both inside and outside of the quantum dot.

than exact integration, given a fixed accuracy requirement. For example, to reach an accuracy better than 10^{-6}, the approximate integration will be 131 times faster than the exact integration.

In general, assembling and solving the system require $O(N^2)$ and $O(N^3)$ operations, respectively. In this example, most of the CPU time was consumed in the assembling process, because of the small number of unknowns. Since the two integration methods affect only the assembling time, the difference of the CPU time would reduce if the number of unknowns increase. However, approximate integration yields a diagonal mass matrix and more sparse stiffness matrices, giving further improvement in the CPU time over exact integration. As such, approximate integration is used in the following examples.

To compare the efficiency and the accuracy of the SEM and FEM, the required CPU time and memory for an accuracy better than 1% for the fundamental eigenvalue are compared in Table II. The conventional FEM requires 245 times more CPU time and 652 times more memory than SEM.

The second example is a homogeneous sphere model of $a = 1\ \mathrm{nm}$ in a radius with $V = 0$ inside the sphere. The analytic eigenvalues of this model are the zeros of the spherical Bessel function

$$j_n(ka) = 0, \qquad n = 0, 1, 2, \ldots \tag{28}$$

where $k = \pi\sqrt{m(E - V)}$. Table III shows the lowest ten eigenvalues by means of analytical solution. In the SEM, the sphere is divided by seven (curved) elements as shown in Fig. 4. We analyzed the sphere model with geometrical orders from $M_\xi = M_\eta = M_\zeta = 2$ to $M_\xi = M_\eta = M_\zeta = 9$ and interpolation orders $N_\xi = N_\eta = N_\zeta = 1$ to $N_\xi = N_\eta = N_\zeta = 9$ (the so-called p-refinement) for each geometrical order, requiring 72 different eigenvalue calculations. Fig. 5 shows errors of the fundamental eigenvalue calculated by the SEM. We observe that the error is below 1% for the fourth-order basis function with the second-order geometrical modeling, or the third-order basis functions with third-order geometrical modeling, or the second-order basis functions with higher than third-order geometrical modeling. We also note that the convergence properties with respect to the interpolation orders depend on the geometrical orders. For example, the error of the fifth-order geometrical modeling does not decrease anymore after the sixth-order basis functions. Therefore, the accuracy of SEM is limited by geometrical orders due to the inherent geometrical error of the model. In other words, the p-refinement can improve the results, but its accuracy is limited by an inherent geometrical model error.

The errors of higher eigenvalues of the sphere model for some higher geometrical orders are also shown in Fig. 6. Similar to the fundamental mode, the errors are limited at 0.3% for third-order geometrical modeling and 0.03% for fifth-order geometrical modeling, whereas errors decrease exponentially with the interpolation orders for the ninth-order geometrical modeling.

It is noted that the geometrical orders are entirely independent of the interpolation orders. Therefore, as the order of geometrical modeling increases, the number of unknowns will not

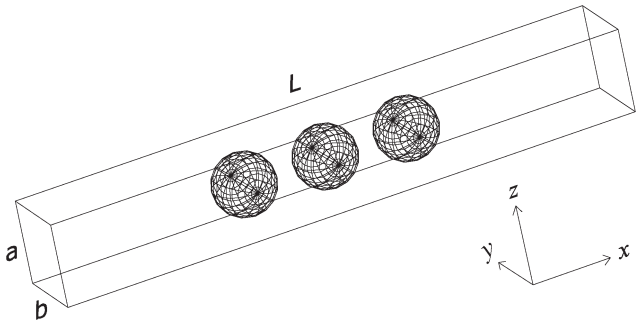

Fig. 10. Geometry of a rectangular waveguide with three spherical quantum dots. The dimensions of the waveguide are $a = 2$ nm, $b = 2$ nm, and $L = 14$ nm. The radius of the quantum dots is 0.75 nm and the distance between quantum dots is 1 nm. The normalized potential is 0 and 2 inside and outside the quantum dots, respectively. Geometrical orders are $(M_\xi = M_\eta = M_\zeta) = 6$ for curved elements and $(M_\xi = M_\eta = M_\zeta) = 1$ for straight orthogonal elements.

increase; it merely requires more CPU time for the calculation of Jacobian matrices. In other words, increasing the geometrical orders of a curved structure can give more accurate results with little increase in the total CPU time.

B. A Quantum Dot

Next, consider a cubic quantum dot shown in Fig. 7. The dimension of the quantum dot is $1\ \text{nm} \times 1\ \text{nm} \times 1\ \text{nm}$ with the potential $V = 0$ and the normalized effective mass $m = 2$, and is surrounded by a cube of dimension $3\ \text{nm} \times 3\ \text{nm} \times 3\ \text{nm}$, with $V = 2$ and $m = 1$. Wave functions on the outer boundary are assumed zero. This problem does not have an analytical solution, so a high-order result $(N_\xi = N_\eta = N_\zeta = 5)$ serves as a reference. The model is divided into 27 elements with an orthogonal mesh. Fig. 8 shows the relative errors of eigenvalues for several modes. Since eigenvalues of mode 2, mode 3, and mode 4 are the same, only mode 1, mode 4, and mode 8 are considered in the calculation of errors.

Fig. 9 shows eigenvectors obtained by using (11) at the center of the xy plane $(z = 1.5\ \text{nm})$.

C. Quantum Dots in a Waveguide

Finally, we considered a rectangular waveguide of length $L = 14$ nm with three spherical quantum dots, as illustrated in Fig. 10. The potential function $V = 0$ for the quantum dots, and $V = 2$ in the surrounding waveguide; the outer boundary of the waveguide walls satisfies the Dirichlet boundary condition. Geometrical orders $M_\xi = M_\eta = M_\zeta = 6$ is used for curved elements and $M_\xi = M_\eta = M_\zeta = 1$ for straight orthogonal elements. An electron beam is propagating along a straight rectangular waveguide (x direction) with the fundamental guided mode. The incident electron wave is described by φ^{inc}. The centers of quantum dots are located at $(x, y, z) = (5, 1, 1)$, (7,1,1), and (9,1,1), respectively. In quantum-dot device design, determination of the reflected and transmitted portions of electrons is very important. In this configuration, we assume that the incoming electron energy E is low enough that only the dominant mode can propagate along the waveguide. The electron wave can be expressed as the summation of the incident and reflected waves as

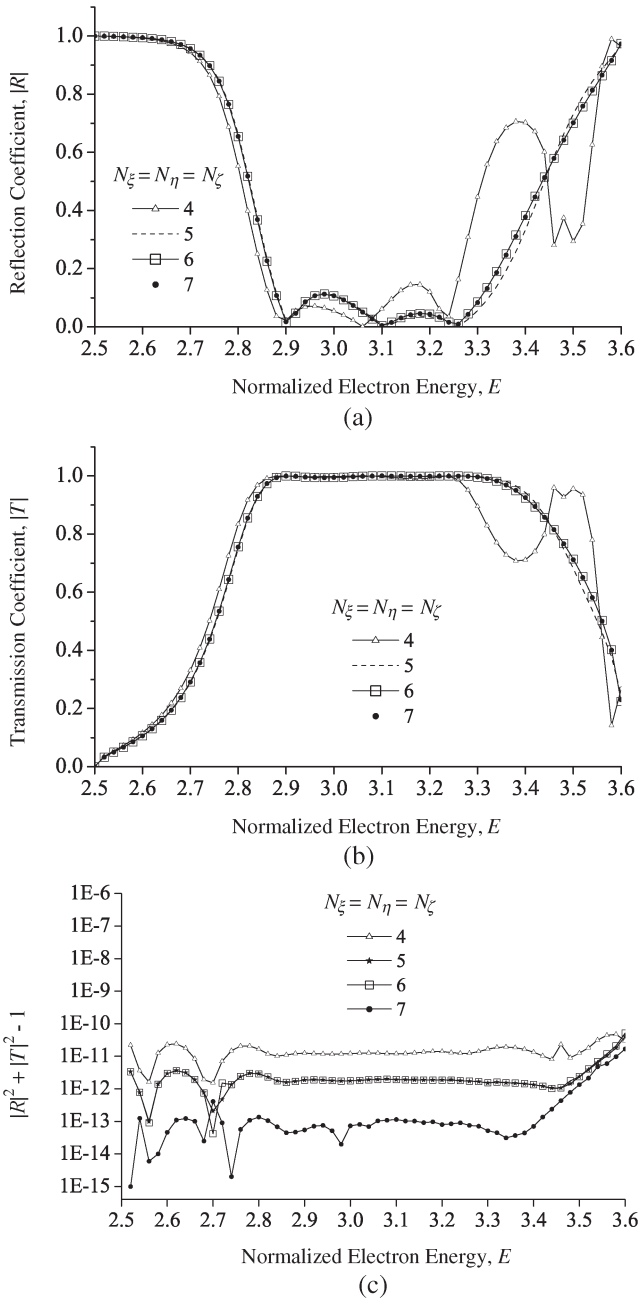

Fig. 11. (a) Reflection and (b) transmission coefficients as functions of the normalized electron energy. (c) Error of $|R|^2 + |T|^2 - 1$.

$$\begin{aligned}\varphi &= \varphi^{\text{inc}} + \varphi^{r} \\ &= \varphi_0 \mathrm{e}^{-jk_x x} + R\varphi_0 \mathrm{e}^{jk_x x}, \qquad x \le 0 \end{aligned} \tag{29}$$

to the left of the waveguide, where R is the reflection coefficient, $k_x = \pi\sqrt{m(E - V) - [(1/a^2) + (1/b^2)]}$ is the propagation constant along the waveguide, and φ_0 is given by

$$\varphi_0(y, z) = \sin\left(\frac{\pi y}{a}\right) \sin\left(\frac{\pi z}{a}\right). \tag{30}$$

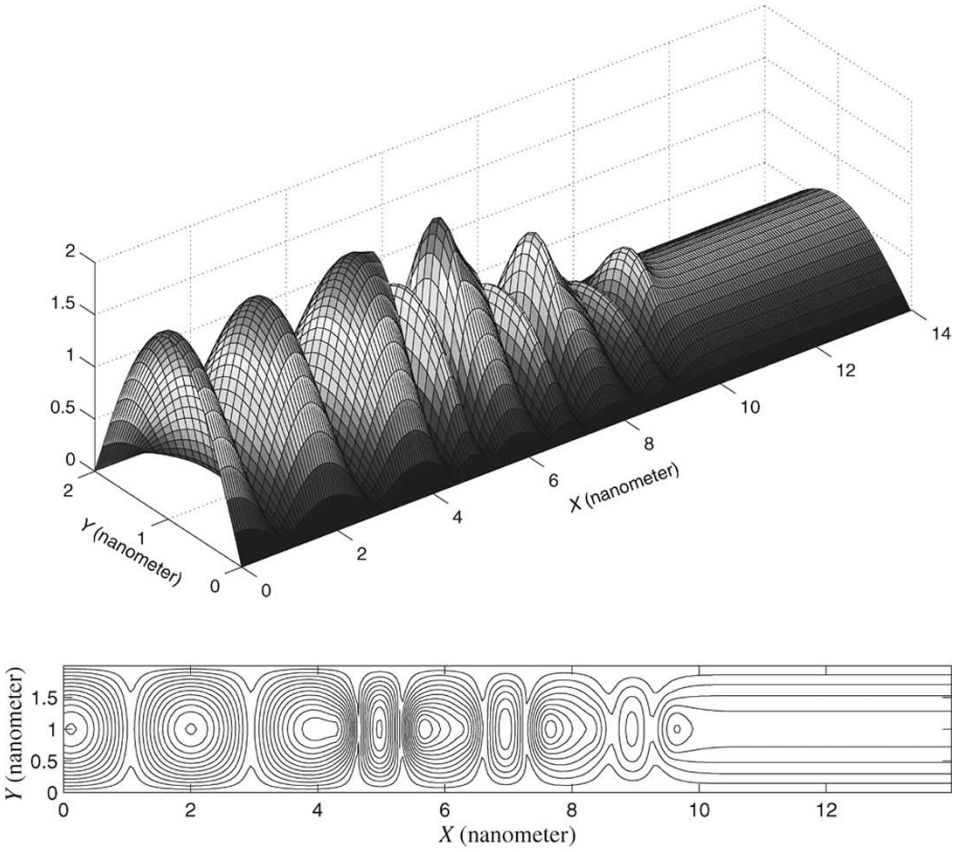

(a)

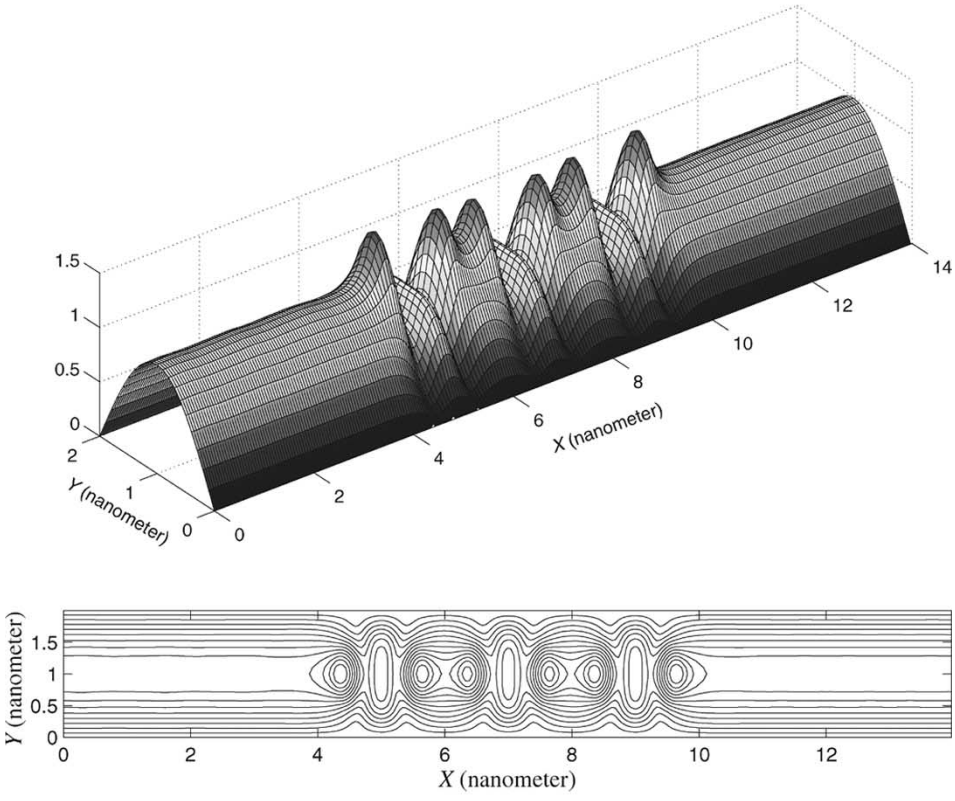

(b)

Fig. 12. Contours of wave function on the xy plane ($z = 1$ nm). Interpolation orders $N_\xi = N_\eta = N_\zeta = 6$. At the given normalized electron energy, (a) $E = 2.78$ and $|R| = 0.654$, $|T| = 0.756$; or (b) $E = 3.10$ and $|R| = 0$, $|T| = 1$.

Similarly, the transmitted wave to the right of the waveguide can be expressed as

$$\begin{aligned}\varphi &= \varphi^t \\ &= T\varphi_0 \mathrm{e}^{-jk_x x}, \qquad x \geq L \end{aligned} \tag{31}$$

where T is the transmission coefficient.

To apply the boundary condition (2), we took the derivative of (29) with respect to x as

$$\frac{\partial \varphi}{\partial x} = jk_x\varphi - 2jk_x\varphi_0 \mathrm{e}^{-jk_x x}. \tag{32}$$

Similarly, we obtained the boundary condition of (31) as

$$\frac{\partial \varphi}{\partial x} = -jk_x\varphi. \tag{33}$$

Substituting (32) and (33) into (2) and (15), together with the Dirichlet boundary condition on the waveguide walls, one can obtain final (17) for the analysis of this waveguide model.

We analyzed this problem with basis functions of order from $N_\xi = N_\eta = N_\zeta = 4$ to $N_\xi = N_\eta = N_\zeta = 7$, in the range of normalized eigenenergy from 2.52 to 3.60 with an increment of 0.02. The number of unknowns for each interpolation orders are 7589, 15 216, 26 755, and 43 016, respectively.

Once the wave function has been found, the reflection and transmission coefficient can be calculated as

$$R = \frac{4}{ab}\int \varphi^r(x_1, y, z)\varphi_0(y, z)\mathrm{d}y\mathrm{d}z \tag{34}$$

$$T = \frac{4}{ab}\int \varphi^t(x_2, y, z)\varphi_0(y, z)\mathrm{d}y\mathrm{d}z \tag{35}$$

where $x_1 = 0$ denotes the position where the wave is incident, and $x_2 = L$ denotes the position where the wave is transmitted.

Fig. 11 gives the magnitudes of the reflection and transmission coefficients as functions of the electron energy. We observe that the two coefficients converge as the order is increased to 6. The reflection and transmission coefficients satisfy $|R|^2 + |T|^2 = 1$. The maximum error of $1 - |R|^2 - |T|^2$ is less than 10^{-10} for all interpolation orders.

Fig. 12 shows contours of the wave functions interpolated on the xy plane ($z = 1$). In general, $R \neq 0$, except for some specific energies. For example, when the normalized eigenenergy is 2.78, wave functions to the left of the quantum dots show the interference pattern between the incident and reflected electronic waves because the reflection coefficient is nonzero at this energy. However, if the normalized eigenenergy $E = 3.10$, the reflection and transmission coefficients are 0 and 1, respectively; thus the magnitudes of the wave functions to the left and to the right of the quantum dots are uniform and are the same as the incident wave. The CPU time for each analysis with interpolation orders $N_\xi = N_\eta = N_\zeta = 6$ is 532 s on a Pentium IV 2.5-GHz computer. The SEM provides an efficient alternative to the finite element and finite difference methods for complex 3-D problems in nanodevice simulation.

V. Conclusion

We have presented an efficient 3-D SEM to solve the Schrödinger equation in nanodevice simulation. The basis functions are the Lagrange–Legendre polynomials on curved hexahedron elements. The geometrical model of curved structures is achieved by high-order polynomials. From the eigenvalue analysis, it is demonstrated that the proposed method gives a spectral accuracy with increasing interpolation orders. In assembling the system matrix, the approximate GLL quadrature integration is superior to exact integration because it gives a diagonal mass matrix and a more sparse stiffness matrix. It is demonstrated that the high-order geometrical model is essential for high accuracy if curved elements are involved. Since geometrical orders are entirely independent of the basis-function orders, increasing the geometrical orders of a curved structure can give more accurate results with little increase in CPU time. Numerical examples demonstrate that the SEM is a highly efficient alternative method for solving the Schrödinger equation in nanodevice simulation. Future research will focus on its application in the self-consistent Schrödinger–Poisson system.

Acknowledgment

The authors wish to thank the reviewers for their constructive comments.

References

[1] D. Bimberg, M. Grundmann, and N. N. Ledentsov, *Quantum Dot Heterostructures*. New York: Wiley, 1999.

[2] D. Vasileska, M. N. Wybourne, S. M. Goodnick, and A. D. Gunther, "3D simulation of GaAs/AlGaAs quantum dot point contact structures," *Semicond. Sci. Technol.*, vol. 13, no. 8, pp. A37–A40, 1998.

[3] A. Thean and J. P. Leburton, "Stark effect and single-electron charging in silicon nanocrystal quantum dots," *J. Appl. Phys.*, vol. 89, no. 5, pp. 2808–2815, 2001.

[4] M. G. Pala and G. Iannaccone, "A three-dimensional solver of the Schrödinger equation in momentum space for the detailed simulation of nanostructures," *Nanotechnology*, vol. 13, no. 3, pp. 369–372, 2002.

[5] J. S. de Sousa, A. V. Thean, J. P. Leburton, and V. N. Freire, "Three-dimensional self-consistent simulation of the charging time response in silicon nanocrystal flash memories," *J. Appl. Phys.*, vol. 92, no. 10, pp. 6182–6187, Nov. 15, 2002.

[6] S. Datta, "Nanoscale device modeling: The Green's function method," *Superlattices Microstruct.*, vol. 28, no. 4, pp. 253–278, Oct. 2000.

[7] R. Ravishankar, P. Matagne, J. P. Leburton, R. M. Martin, and S. Tarucha, "Three-dimensional self-consistent simulations of symmetric and asymmetric laterally coupled vertical quantum dots," *Phys. Rev. B*, vol. 69, no. 3, Art. No. 035326, Jan. 2004.

[8] E. J. Austin and M. Jaros, "Electronic structure of an isolated GaAs-GaAlAs quantum well in a strong electric field," *Phys. Rev. B*, vol. 31, no. 8, pp. 5569–5572, Apr. 1985.

[9] D. A. B. Miller, D. S. Chemla, T. C. Damen, A. C. Gossard, W. Wiegmann, T. H. Wood, and C. A. Burrus, "Electric field dependence of optical absorption near the band gap of quantum-well structures," *Phys. Rev. B*, vol. 32, no. 2, pp. 1043–1060, Jul. 1985.

[10] D. Ahn and S. L. Chuang, "Exact calculation of quasi-bound states of an isolated quantum-well with uniform electric-field-quantum-well Stark resonance," *Phys. Rev. B*, vol. 34, no. 12, pp. 9034–9037, Dec. 1986.

[11] D. M.-T. Kuo and Y. C. Chang, "Dynamic behavior of electron tunneling and dark current in quantum well systems under an electric field," *Phys. Rev. B*, vol. 60, no. 23, pp. 15957–15964, Dec. 1999.

[12] S. Panda and B. K. Panda, "Analytic methods for field induced tunneling in quantum wells with arbitrary potential profiles," *Pramana, J. Phys.*, vol. 56, no. 6, pp. 809–822, Jun. 2001.

[13] G. Bastard, E. E. Mendex, L. L. Chang, and L. Esaki, "Variational calculations on a quantum well in an electric field," *Phys. Rev. B*, vol. 28, no. 6, pp. 3241–3245, Sep. 1983.
[14] K. Nakamura, A. Shimizu, M. Koshiba, and K. Hayata, "Finite-element analysis of quantum wells of arbitrary semiconductors with arbitrary potential profiles," *IEEE J. Quantum Electron.*, vol. 25, no. 5, pp. 889–895, May 1989.
[15] C. Juang, K. J. Kuhn, and R. B. Darling, "Stark shift and field-induced tunneling in $Al_xGa_{1-x}As/GaAs$ quantum-well structures," *Phys. Rev. B*, vol. 41, no. 17, pp. 12047–12053, Jun. 1990.
[16] S. Panda, B. K. Panda, S. Fund, and C. D. Beling, "Electric field effect on the diffusion modified AlGaAs/GaAs single quantum well," *J. Appl. Phys.*, vol. 80, no. 3, pp. 1532–1540, Aug. 1996.
[17] S. Glutsch and D. S. Chemla, "Numerical calculation of the optical absorption in semiconductor quantum structures," *Phys. Rev. B.*, vol. 54, no. 16, pp. 11592–11601, Oct. 1996.
[18] P. Harrison, *Quantum Wells, Wires, and Dots—Theoretical and Computational Physics*. Chichester, U.K.: Wiley, 2000.
[19] S. L. Chuang, S. Schimitt-Rink, D. A. B. Miller, and D. S. Chemla, "Exciton Green's-function approach to optical absorption in a quantum well with an applied electric field," *Phys. Rev. B*, vol. 43, no. 2, pp. 1500–1509, Jan. 1991.
[20] J. A. Proto, J. Sánchez-Dehesa, L. A. Cury, S. Nogare, and J. C. Portal, "Left and right tunneling times of electrons from quantum wells in double-barrier heterostructures investigated by the stabilization method," *J. Phys. Condens. Matter*, vol. 6, no. 4, pp. 887–898, Jan. 1994.
[21] S. Panda, B. K. Panda, and S. Fung, "Application of Fourier series methods for studying tunneling of electrons out of quantum wells in an electric field," *J. Phys. Condens. Matter*, vol. 11, no. 27, pp. 5293–5312, Jul. 1999.
[22] M. Bylecki, W. Jaskolsky, and R. Oszwaldowsky, "Resonant tunneling lifetimes in multi-barrier structures—A complex coordinate approach," *J. Phys. Condens. Matter*, vol. 8, no. 35, pp. 6393–6404, Aug. 1996.
[23] M. L. Zambrano and J. C. Arce, "Stark-resonance densities of states, eigenfunctions, and lifetimes for electrons in GaAs/(Al, Ga)As quantum wells under strong electric fields: An optical-potential wave packet propagation method," *Phys. Rev. B*, vol. 66, no. 15, pp. 155340–155348, Oct. 2002.
[24] Q. H. Liu, C. Cheng, and H. Z. Massoud, "The spectral grid method: A novel fast Schrödinger-Equation solver for semiconductor nanodevice simulation," *IEEE Trans. Comput.-Aided Des. Integr. Circuits Syst.*, vol. 23, no. 8, pp. 1–9, Aug. 2004.
[25] Q. H. Liu, "A pseudospectral frequency-domain (PSFD) method for computational electromagnetics," *IEEE Antennas Wireless Propagat. Lett.*, vol. 1, no. 6, pp. 131–134, 2002.
[26] C. Cheng, Q. H. Liu, and H. Z. Massoud, "Spectral element method for the Schrödinger–Poisson system," in *Int. Workshop Computational Electronics (IWCE-10)*. West Lafayette, IN: Purdue Univ., Oct. 24–27, 2004, pp. 221–222.
[27] Q. H. Liu, "The PSTD algorithm: A time-domain method requiring only two cells per wavelength," *Microw. Opt. Technol. Lett.*, vol. 15, no. 3, pp. 158–165, 1997.
[28] B. Yang, D. Gottlieb, and J. S. Hesthaven, "Spectral simulation of electromagnetic wave scattering," *J. Comput. Phys.*, vol. 134, no. 2, pp. 216–230, 1997.
[29] B. Tian and Q. H. Liu, "Nonuniform fast cosine transform and Chebyshev PSTD algorithm," *Prog. Electromagn. Res.*, vol. PIER 28, pp. 259–279, 2000.
[30] D. Komatitsch, C. Barnes, and J. Tromp, "Wave propagation near a fluid-solid interface: A spectral-element approach," *Geophysics*, vol. 65, no. 2, pp. 623–631, Mar.–Apr. 2000.
[31] G.-X. Fan, Q. H. Liu, and J. S. Hesthaven, "Multidomain pseudospectral time-domain method for simulation of scattering from buried objects," *IEEE Trans. Geosci. Remote Sens.*, vol. 40, no. 6, pp. 1366–1373, Jun. 2002.
[32] G. Zhao and Q. H. Liu, "The 2.5-D multidomain pseudospectral time-domain algorithm," *IEEE Trans. Antennas Propag.*, vol. 51, no. 3, pp. 619–627, Mar. 2003.
[33] J.-H. Lee and Q. H. Liu, "Analysis of 3D eigenvalue problems based on a spectral element method," in *Int. Union Radio Science (URSI) Meeting Abstract*, Monterey, CA, Jun. 2004, p. 30.
[34] W. H. Press, B. P. Flannery, S. A. Teukolsky, and W. T. Vetterling, *Numerical Recipes*. New York: Cambridge Univ. Press, 1989.
[35] M. Milan and M. Branislav, "Higher order hierarchical curved hexahedral vector finite elements for electromagnetic modeling," *IEEE Trans. Microw. Theory Tech.*, vol. 51, no. 3, pp. 1026–1033, Mar. 2003.
[36] D. Gottlieb and S. A. Orszag, *Numerical analysis of Spectral Methods*. Philadelphia, PA: SIAM, 1977.
[37] C. Canuto, M. Y. Hussani, A. Quarteroni, and T. Zang, *Spectral Methods in Fluid Dynamics*. New York: Springer-Verlag, 1988.
[38] B. Fornberg, *A Practical Guide to Pseudospectral Methods*. New York: Cambridge Univ. Press, 1996.
[39] J. P. Boyd, *Chebyshev and Fourier Spectral Methods*. New York: Dover, 2001.

Joon-Ho Lee received the Ph.D. degree in electrical engineering from Dankook University, Seoul, Korea, in 1999.

He was, from January 2000 to February 2002, a Postdoctoral Research Associate with the School of Information and Communication Engineering, Sungkyunkwan University, Suwon, Korea, and from March 2002 to October 2003, a Research Assistant Professor. He is currently a Postdoctoral Research Associate at the Department of Electrical and Computer Engineering, Duke University, Durham, NC. His research interests include computational electromagnetics, optimal design of electromagnetic devices, and electromechanical coupled systems.

Qing Huo Liu (S'88–M'89–SM'94–F'05) received the Ph.D. degree in electrical engineering from the University of Illinois, Urbana-Champaign, in 1989.

He was with the Electromagnetics Laboratory at the University of Illinois, Urbana-Champaign, as a Research Assistant from September 1986 to December 1988, and as a Postdoctoral Research Associate from January 1989 to February 1990. He was a Research Scientist and Program Leader with Schlumberger–Doll Research, Ridgefield, CT, from 1990 to 1995. From 1996 to May 1999, he was an Associate Professor with New Mexico State University, Las Cruces, NM. Since June 1999, he has been with Duke University, where he is now a Professor of Electrical and Computer Engineering. His research interests include computational electromagnetics and acoustics, inverse problems, geophysical subsurface sensing, biomedical imaging, electronic packaging, and the simulation of photonic and nano devices. He has published more than 290 papers in refereed journals and conference proceedings.

Dr. Liu is a member of Phi Kappa Phi, Tau Beta Pi, SEG, a full member of the US National Committee of URSI Commissions B and F. Currently, he serves as an Associate Editor for *Radio Science*, and for IEEE TRANSACTIONS ON GEOSCIENCE AND REMOTE SENSING, for which he also served as a Guest Editor for a special issue on computational methods. He received the 1996 Presidential Early Career Award for Scientists and Engineers (PECASE) from the White House, the 1996 Early Career Research Award from the Environmental Protection Agency, and the 1997 CAREER Award from the National Science Foundation.